Shadow Imaging of Geostationary Satellites: silhouette reconstruction from accurate polychromatic modelling of diffraction and atmospheric disturbances

Hanae Labriji, Olivier Herscovici-Schiller, Frédéric Cassaing

Shadow Imaging of Geostationary Satellites: silhouette reconstruction from accurate polychromatic modelling of diffraction and atmospheric disturbances

Hanae Labriji[⋆†]*, Olivier Herscovici-Schiller*[⋆] *and Frédéric Cassaing*[⋆]
[⋆] *DTIS, ONERA, Université Paris Saclay,*
F-91123 Palaiseau - France
hanae.labriji@onera.fr ··· olivier.herscovici@onera.fr ··· frederic.cassaing@onera.fr
[†]Corresponding author

June 2022

Abstract

Shadow imaging is a very promising technique for imaging the silhouette of geostationary satellites at submetric resolutions from the ground. The method is based on the numerical inversion of the shadow cast by the satellite when it occults a star. We have built an inversion algorithm based both on a fine physical modelling of light propagation, and that makes full use of the polychromatic flux of the star. We conducted several simulations to show a few realistic working examples, giving special attention to shadow sampling. We also proved that the chromatic inversion allows for a considerable improvement in the reconstruction.

1. Introduction

1.1 Context

Because of their high launching and manufacturing costs, and in order to extend their lifetime as much as possible, the resolved imaging of geostationary and geosynchronous satellites is gaining more and more interest over the scientific space surveillance community. Geostationary satellites also play an increasingly crucial role in several fields including modern communication, Earth observation and weather forecasting. Yet these several hundred satellites are out of range of the biggest ground-based telescopes due to their size and distance from Earth. For instance, using one of the biggest existing apertures of diameter $D = 10\,\mathrm{m}$ coupled with adaptive optics at a wavelength $\lambda = 1.25\,\mu\mathrm{m}$ gives a spatial resolution on the satellite of only 4.5 meters[1] , which barely enables the body of the satellite to be distinguished from the solar panels. In fact, imaging a geostationary satellite to a sub-metric resolution requires an angular resolution of just a few milli-arcseconds, and hence a diffraction-limited optical aperture of several tens of meters.

Many other methods have been considered to resolve geostationnary satellites such as Fourier telescopy[2] and interferometry, based on the coherent recombination of the beams of a deca- to hectometric array of telescopes either fixed on the ground,[3] or on a pointed platform[4] or mobile and connected by optical fibres.[5] The main practical limitation of interferometry is the fact that satellites are most of the time very faint targets (12th-14th magnitude[6]) difficult to detect by the usual interferometers. The only observations reported in the literature occur during glint (a bi-annual phenomenon where, due to the direct reflection of sunlight by the satellite, the latter becomes very bright (of 7th-8th magnitude)).[6–8] Alternatively, the Magdalena Ridge Observatory Interferometer is highly promising and has been designed to track such faint targets,[9] but to date no such detection has been reported in the literature.

This work deals with an unconventionnal optical imaging method named shadow imaging, an innovative and cost effective technique suggested by Burns and colleagues in 2 005.[10] Shadow imaging may provide the sub-metric contour of a space object from the shadow it casts when occulting a star. The shadow encodes the information of the satellite's contour, an inverse problem must be solved to retrieve it. The scientific processing of occultation data is not a new fancy idea. On the contrary, it has found several applications for ground-based observations of solar system features[11] and has become commonplace to measure the diameter of asteroids.[12]

In this work, we will focus on optical aspects involving the modelling of the starlight path and the inverse problem. We will start by exposing the working principle of the method, then we will describe the forward physical model in Section 2. In Section 3, we will deal with the dimensioning of the detector, by calculating the size of the telescope

array and the spacing between them. We will afterwards build an inversion algorithm and assess its performance in Section 4.

1.2 Principle

The principle of shadow imaging of geostationnary satellites is depicted in Fig. 1. Due to the apparent motion of the star caused by Earth's rotation, the shadow moves from west to east at a speed between 2700 m/s and 3500 m/s, depending on the longitude of the satellite and the latitude of the observer. This high speed requires a very fast acquisition rate, but allows the 2D diffraction pattern of the satellite to be efficiently acquired by a single row of telescope. For instance, the digital acquisition of the cast shadow is performed using a row of small telescopes placed perpendicular to the estimated trajectory of the shadow. Thus, at each moment of the occultation, a line of the 2D shadow image will be recorded. Each telescope acts as a light collecting bucket, delivering the value of one pixel per line. The superposition of all the acquired lines reveal the complete 2D image of the satellite's shadow. Unlike classical methods that rely on the optical combination of coherent light beams collected over one or several apertures, shadow imaging relies on the much simpler electronic processing of light collected by the array of telescopes. In addition to generating cost savings by using on-the-shelf telescopes, it significantly reduces the complexity of the optical assembly.

As can be seen in Fig. 1, the collected shadow does not correspond to the perfect geometrical contour of the satellite, making it necessary to solve an inverse problem based on a very fine knowledge of the complete propagation chain. The major physical phenomenon at play is light diffraction, and the shadow recorded is mainly the diffraction pattern produced by the obstacle. Along its path through the Earth's atmosphere, diffracted light undergoes two main disturbances. The first effect is atmospheric refraction, which induces a chromatic shift that blurs the image of the shadow. The second effect is atmospheric scintillation, which causes a random variation in the intensity received by the collecting sub-apertures. Both of these effects must be taken into account in the simulation of the starlight path.

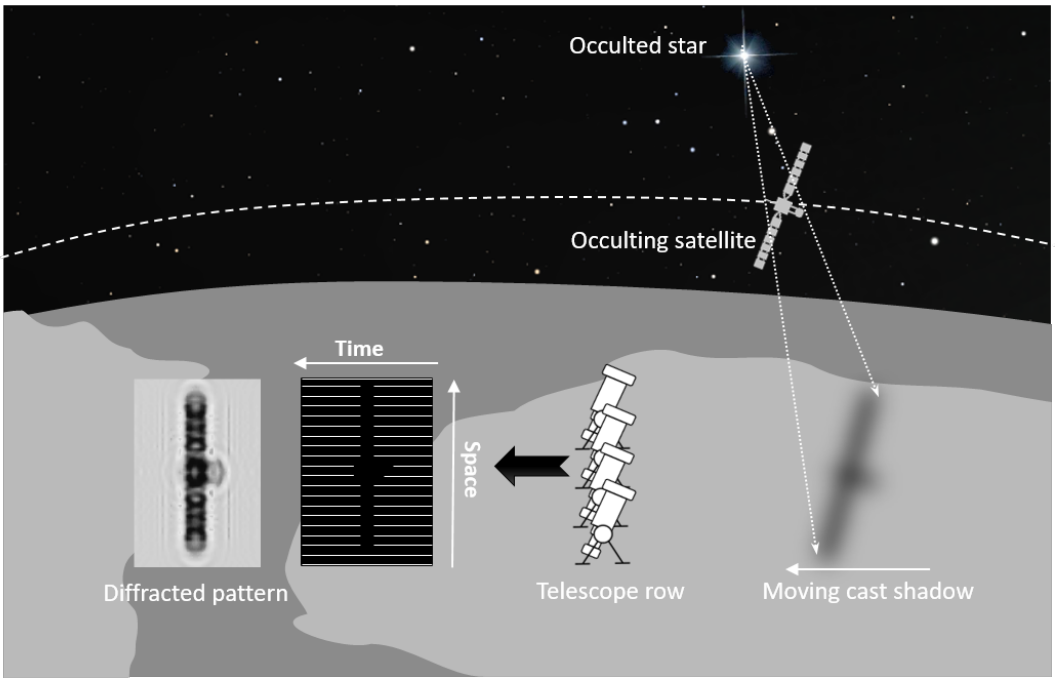

Figure 1: Principle of shadow imaging of geostationary satellites.

Shadow imaging of geostationary satellites is nonetheless a very challenging method since the placement of the telescope array depends on an accurate estimation of the shadow position in the ground, which is itself tightly linked to a precise estimation of satellite trajectory. Many prior publications have tackled this issue.[13–16] In his work,[16] Sheppard showed that the characterisation of the position of satellites using the Two Line Element set was far from being sufficient to achieve reasonable uncertainties on the position of the shadow on the ground. For example the error on the north-south shadow position is found to reach 1 to 2 kilometres. The practical execution of shadow imaging is therefore closely linked to the precise estimation of the position of the satellite of interest.

2. Forward problem : modelling the light path of the starlight

2.1 Light diffraction

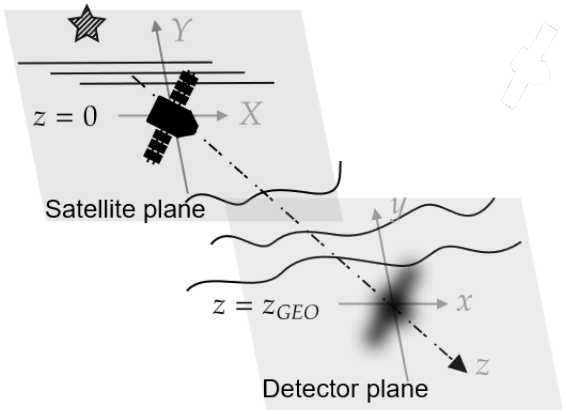

Figure 2: Geometric notations.

A successful and efficient reconstruction of the satellite silhouette from its shadow requires the fine knowledge of each part of the transmission chain, starting from the star and ending at the detector plane. As we stated before, the main contributor is the diffraction of the starlight after encountering the obstacle. It is mathematically described by the Huygens-Fresnel integral coupled with the paraxial approximation. As sketched in Fig. 2, (X, Y) and (x, y) are, respectively, the coordinates at the satellite plane and at the observer plane while z is the coordinate on the optical axis star-satellite-observer, z equals zero on the satellite plane and z_{GEO} at the observer plane. A wave U_0 propagated to a distance z is given by:[17]

$$U_z(x,y) = \frac{\exp(\mathrm{i}kz)}{\mathrm{i}\lambda z} \iint_{-\infty}^{\infty} U_0(X,Y) \exp\left[\mathrm{i}\frac{k}{2z}\left((X-x)^2 + (Y-y)^2\right)\right] \mathrm{d}X\mathrm{d}Y, \tag{1}$$

where λ is the observation wavelength and $k = 2\pi/\lambda$ is the wave number.

The shape of the diffracted wave mainly depends in a quantity called the Fresnel number N_F and defined as:

$$N_F = \frac{T^2}{\lambda z}, \tag{2}$$

where T is the maximum size of the satellite in both dimensions. When the Fresnel number is small compared to 1, the diffraction is said to be in the far-field or in the Fraunhofer regime. The image plane is so distant from the object plane that the wavefront of the wave (Eq (1)) can be approximated by a plane wavefront, so the angular shape of the diffracted wave no longer depends on the parameters λ and z.

From the point of view of an observer in metropolitan France, geostationary satellites are about 40,000 km from the ground and are typically between 10 and 20 metres in size, the associated Fresnel numbers at $\lambda_0 = 550\,\mathrm{nm}$ are between 5 and 20, they therefore diffract in the Fresnel regime and their diffraction pattern depends strongly on the propagation distance and the observation wavelength.

Assuming that the occulted star is a point source, the incident wave is simply a plane wave, and thus U_0 can be defined, apart from a multiplicative phase term, as the satellite transmission function: zero on the satellite support and 1 everywhere else. In order to avoid the two infinite-bound integrals, a simple trick is to use the Babinet principle[18] and decompose the integral into two parts:

$$\begin{aligned} U_z(x,y) = {} & \frac{\exp(\mathrm{i}kz)}{\mathrm{i}\lambda z} \iint_{-\infty}^{\infty} \exp\left[\mathrm{i}\frac{k}{2z}\left((X-x)^2 + (Y-y)^2\right)\right] \mathrm{d}X\mathrm{d}Y \\ & - \frac{\exp(\mathrm{i}kz)}{\mathrm{i}\lambda z} \iint_{-T/2}^{T/2} \overline{U_0}(X,Y) \exp\left[\mathrm{i}\frac{k}{2z}\left((X-x)^2 + (Y-y)^2\right)\right] \mathrm{d}X\mathrm{d}Y. \end{aligned} \tag{3}$$

The first part of Eq. 3 is simply a propagated plane wave (that is a plane wave also). The second one, denoted $\overline{U_z}$ in the following, is a finite-bound integral that represent the propagation of an object complementary to the satellite.

The second integral has to be computed numerically for each set of parameters. Even in very simple special cases there is no analytical solution to this integral and therefore it has to be solved numerically. There are several ways of calculating this integral,[17] the most frequently used are either convolving the incident wave U_s with the Fresnel kernel $K(x, y)$ (and its bounded kernel version[19]):

$$K(x, y) = \exp\left[\mathrm{i}\frac{k}{2z}\left(x^2 + y^2\right)\right], \tag{4}$$

such as:

$$\overline{U}_z(x, y) = \overline{U_0} * K(x, y). \tag{5}$$

Or performing a direct Fourier transform (denoted by $\mathbb{FT}$ below), noticing that:

$$\overline{U}_z(x, y) = \frac{\exp(\mathrm{i}kz)}{\mathrm{i}\lambda z}\exp\left[\mathrm{i}\frac{\pi}{\lambda z}\left(x^2 + y^2\right)\right]\mathbb{FT}\left\{(X, Y) \mapsto \overline{U_0}(X, Y)\exp\left[\mathrm{i}\frac{\pi}{\lambda z}\left(X^2 + Y^2\right)\right]\right\}\left(\frac{x}{\lambda z}, \frac{y}{\lambda z}\right). \tag{6}$$

These two methods are the most used because they are based on the Fast Fourier Transform (FFT) algorithm. However, they have several disadvantages, such as the strict constraints applied to sampling in both the object and image planes.[20,21] In the numerical model that will provide the basis for our reconstruction algorithm, we choose to rely on a modal approach, which allows us to obtain a continuous solution at each propagation distance. For this purpose, we use the set of Hermite-Gauss (HG) functions $(\psi_n)_{n\in\mathcal{N}}$;[22] an orthonormal basis of gaussian modes that are analytical solutions of the wave equation in the paraxial approximation,[23] defined as:

$$\psi_n(x, z, W(z), R(z)) = \frac{H_n(\sqrt{2}x/W)}{\sqrt{2^{n+1/2}n!\sqrt{\pi}W}}\exp\left(-\frac{x^2}{W^2}\right)\exp\left[-jk\frac{x^2}{2R} + j\phi_n(W, R)\right], \tag{7}$$

where H_n is the Hermite polynomial of order n, the waist $W(z)$ follows:

$$W^2(z) = W_0^2\left[1 + \left(\frac{\lambda z}{\pi W_0^2}\right)^2\right], \tag{8}$$

and $R(z)$ is the phase front radius of curvature:

$$R(z) = z\left[1 + \left(\frac{\pi W_0^2}{\lambda z}\right)^2\right], \tag{9}$$

ϕ_n is known as the Gouy phase, given by:

$$\phi_n(W, R) = \left(n + \frac{1}{2}\right)\tan^{-1}\left(\frac{\pi W^2}{\lambda R}\right). \tag{10}$$

The idea is then to simply decompose the initial object in the HG basis, to analytically propagate these functions and then to reconstruct the diffraction pattern at each chosen distance z.

In order to perform these calculations numerically, one needs to choose an initial waist W_0 and the maximum number of modes M. While there are several ways to choose these two parameters,[24] a good trade-off between the spatial extent of the object T and its sampling step δX is to take:

$$W_0 = \sqrt{\frac{T\delta X}{\pi}}, \tag{11}$$

$$M = \left\lfloor\left(\frac{T}{2W_0}\right)^2\right\rfloor. \tag{12}$$

2.2 Atmospheric refraction

Atmospheric refraction is a phenomenon caused by the optical index gradient in the Earth's atmosphere, which bends the incident star rays towards the ground according to their wavelength λ and angle of incidence z. As depicted in Fig. 3, its effect on shadow imaging is the chromatic shift $b(\lambda)$ in the position of the satellite shadow on the ground.[13,25] Being wavelength dependent, this shift induces shadow blurring due to the incoherent addition of slightly shifted shadows of different wavelengths.

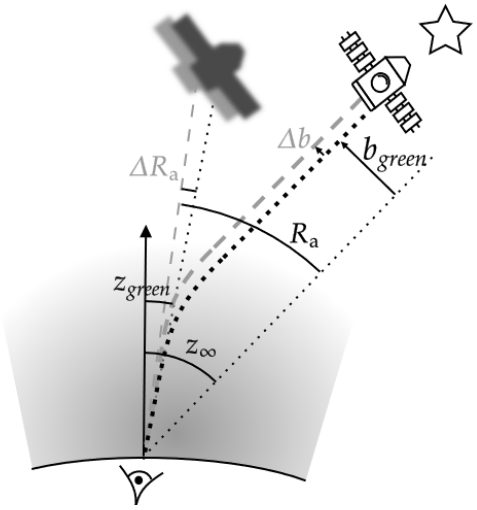

Figure 3: Absolute deviation of lateral shift from its value at $\lambda_0 = 550\,\text{nm}$ as a function of wavelength.

As the fine quantification of this loss is crucial to ensure the feasibility of the method, we have studied the evolution of the lateral displacement as a function of wavelength in the spherical approximation of the Earth (this calculation is usually conducted within the flat earth approximation).[26] The effect of refraction is all the more important for geostationary satellites as they are at a zenith angle of about 45°, refraction being zero at the zenith and increasing sharply with the target's zenith angle. In,[26] we extracted the variation equations of refraction from the geometric tracing of a light ray path. Then we integrated the system of coupled equations using a numerical method and the dry atmosphere model. In addition to this, based on Taylor expansions, we established three analytic approximations of the lateral shift, one of which is the one usually used in the literature. We plotted in Fig. 4 the absolute deviation of the chromatic lateral shit from its value at $\lambda_0 = 550\,\text{nm}$ (center of the V-Band), at a 45° zenith angle:

$$\Delta b_0(\lambda) = b_0(\lambda) - b_0(\lambda_0). \tag{13}$$

We observe that the lateral shift deviation decreases with the wavelength. In consistency with the fact that the refractive index of the atmosphere varies as $1/\lambda^2$, we notice in Fig. 4 that the decrease of Δb is faster in the blue wavelengths than in the red ones. Δb reaches 6 cm at $\lambda = 400\,\text{nm}$ and more than 2 cm at 700 nm. The cut-off frequency (in terms of field and not intensity) for a given spectral bandwidth $\Delta\lambda$ can be approximated as:

$$f_{\text{refr}} \approx 1/\alpha\Delta\lambda, \tag{14}$$

where $\alpha = \mathrm{d}b/\mathrm{d}\lambda$ is wavelength dependent. For instance, at $\lambda_0 = 550\,\text{nm}$, $\alpha_0 = 0.26\,\text{m}/\mu\text{m}$ which yields for $\Delta\lambda = 40\,\text{nm}$ to $f_{\text{refr}} = 96\,\text{m}^{-1}$ that is expected to induce a resolution loss of less than 2 cm. However, for $\Delta\lambda = 400\,\text{nm}$ between 400 nm and 800 nm, assuming a constant $\alpha = 0.26\,\text{m}/\mu\text{m}$, we get a resolution loss of 10 cm, which starts to represent a significant loss of resolution, given the expected resolutions on the object. Hence, we consider the effect of refraction on fringe blurring to be negligible in narrow bandwidths, but to be be taken into account when realigning the shadows of different wavelengths and when calculating the position of the telescopes.

2.3 Atmospheric turbulence: scintillation

Atmospheric turbulence refers to random variations in the optical index of the atmosphere due to the chaotic mixing of air masses. Two different sources of turbulence can be identified. First at the lower altitudes, where turbulence is mainly caused by the ground surface topography and atmospheric convection. And second, at higher altitudes, where it is generated by the wind shears occurring at the interface between two layers of different speed. The main physical manifestation of this phenomena are the Jet-Streams near the tropopause. The small variations of the optical index induce locally (at a given altitude) phase variations of the observed wavefronts, and as the distorted wavefront propagates, the phase variations are converted into amplitude variations; this is what we usually call scintillation.

In conventional imaging, the optical system makes all the coherent incident rays interfere to create the image of the object in the focal plane. In case of atmospheric turbulence, this optical recombination induces a strong loss of resolution described by the Fried parameter r_0 and requires the use of an adaptive-optics system to compensate for the phase distortions. On the contrary, as shadow imaging relies on a simple electronic processing of the telescopes'

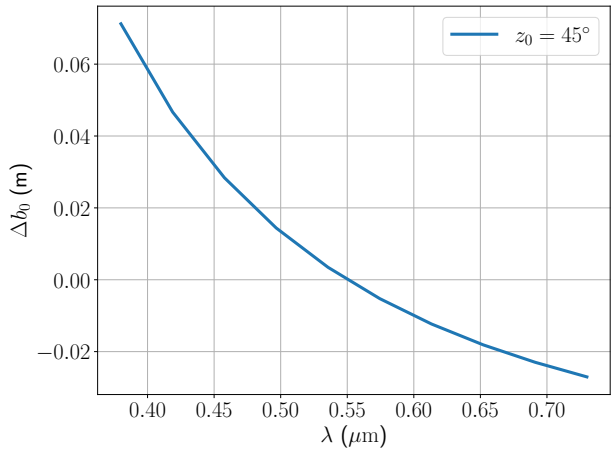

Figure 4: Absolute deviation of lateral shift from its value at $\lambda_0 = 550\,\text{nm}$ as a function of wavelength.

output, each telescope suffers from a sole scintillation effect that induces a small variation in the collected intensity. In the following, we will quantify the variance of scintillation in order to check that it is manageable by the inverse-problem solver.

Authors investigating the effect of turbulence on shadow imaging[13,25] have usually carried out numerical simulations of the propagation of the diffracted wave while placing numerous phase screens to simulate atmospheric turbulence, and then noticing the effect on the reconstructed object. Here, we present an analytical approach to derive the scintillation variance for the parameters involved. We briefly recall hereinafter the mathematical modelling of scintillation exposed in the book[27] by Roddier, based on the Rytov's approximation which assumes that turbulence is a multiplicative perturbation. The scintillation index describes the normalized variance of intensity and is defined as:

$$\sigma_I^2 = \frac{\langle I - \langle I \rangle \rangle^2}{\langle I \rangle^2}. \tag{15}$$

One way to calculate the variance of a statistical process is to study its power spectral density (PSD). We note χ the normalized fluctuation of intensity due to atmospheric turbulence and $W_\chi(\mathbf{f})$ its PSD according to the spatial frequency vector $\mathbf{f} = (f_x, f_y)$. One has:

$$\sigma_I^2 = 4 \int_0^\infty W_\chi(\mathbf{f})\,\mathrm{d}\mathbf{f}. \tag{16}$$

And according to F. Roddier,[27] $W_\chi(\mathbf{f})$ is given by:

$$W_\chi(\mathbf{f}) = 0.38\lambda^{-2} C_N^2(h)\, F(f) \sin^2(\pi\lambda h f^2), \tag{17}$$

where $C_N^2(h)$ is a parameter that describes the local variations of the refractive index on the optical paths, it mainly depends on the altitude of the disturbance. $F(f)$ is the frequency part of the power spectrum density of the refractive index, it is usually given by the Kolmogorov turbulence law $F(f) = f^{-11/3}$.[28] λ is the observation wavelength, and $f = \|\mathbf{f}\|$.

To the previous PSD, it is necessary to add the contribution of the transfer function of the telescope that smooths the high frequencies:[27,29]

$$\mathcal{A}(f) = \left(\frac{2J_1(\pi D f)}{\pi D f} \right)^2, \tag{18}$$

where D is the telescope's diameter and J_1 is the Bessel function of the first kind of order 1.

In order to calculate the variance of the scintillation on each telescope during the shadow's transit, we need to convert the spatial frequencies (f_x, f_y) into a time frequency ν using Taylor's hypothesis. We thus assume that each turbulent layer is translated, unchanged, at a wind velocity V taken along the $\vec{x}$ axis. The last parameter to be taken into account is the short duration (Δt_s) of the acquisition that will change the local average of the intensity and thus decrease the apparent variance of the scintillation.

Taking all these elements into accounts, the spectral power density to be considered for shadow imaging is the following:

$$W_I(\nu, z_0) = \frac{6}{V}\lambda^{-2}\cos^{-3}(z_0)\left(1 - \frac{\sin\pi\nu\Delta t_s}{\pi\nu\Delta t_s}\right)^2 \int_0^\infty \int_0^\infty \left(\frac{J_1(\pi D f)}{\pi D f}\right)^2 f^{-11/3} C_N^2(h) \left(\sin(\pi\lambda h f^2)\right)^2 \mathrm{d}h\,\mathrm{d}f_y, \tag{19}$$

where we integrated along f_y and added the effect of the zenith angle.[30]

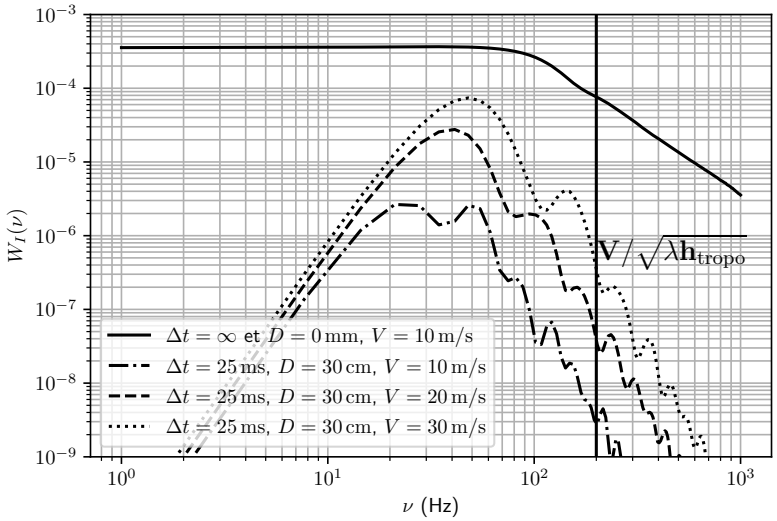

Figure 5: Scintillation power spectral density for various parameters of wind speed.

Fig. 5 shows the evolution of the PSD as a function of the time frequency ν for three different wind speeds. The upper curve relates to turbulence observed over an infinitely long time and integrated over an infinitely small aperture. Since the variance equals the area under each curve, we can see the significant gain due to the short acquisition time and the diameter of the telescope (a few times larger than $\sqrt{\lambda h_{\mathrm{tropo}}}$). Here, we find standard deviations σ_I of 1% at $V = 10\,\mathrm{m/s}$, 3% at $V = 20\,\mathrm{m/s}$ and 6% at $V = 30\,\mathrm{m/s}$. These values are small and are not expected to raise difficulties for the inversion algorithm, due to the spatial averaging of the telescope and the short acquisition time. The PSD computed for $V = 30\,\mathrm{m/s}$ will be used as a reference to further investigate the reliability of the reconstruction algorithm in Section. 4.

3. Shadow detection: sampling and spatial extent

In this section we will establish the useful extent of the shadow and its sampling, aiming at a specific satellite size T and a target resolution ΔX. We start by giving the sampling rules and then study the spatial extension of the shadow. The variables of interest will be related to the physical parameters of the observation (the spectral bandwidth $\Delta\lambda$, the signal to noise ratio (SNR) and the star's magnitude m_{v}). In the following, we consider an object of maximum size T, and we denote by ΔX the resolution to be achieved on the object. The corresponding HG parameters are:

$$W_0 = \sqrt{\frac{T\Delta X}{2\pi}}, \tag{20}$$

$$M = \left\lfloor \left(\frac{T}{2W_0}\right)^2 \right\rfloor. \tag{21}$$

3.1 Sampling pitch

To establish the sampling rules of the shadow, we will consider the 1D case only. There are numerous ways of characterising the frequency of a field resulting from Fresnel diffraction, so many authors simply take the instantaneous frequency of the Fresnel kernel. Here, we choose to make use of the frequency information provided by the HG functions. The instantaneous frequency f_{inst} of the diffracted field $\overline{U_z}$ increases linearly with its distance from the centre x such as:

$$f_{\mathrm{inst}}(x) \leq \frac{\sqrt{M}}{\pi W_{\mathrm{GEO}}} + \frac{x}{R_{\mathrm{GEO}}\lambda_0}, \tag{22}$$

where R_{GEO} and W_{GEO} are given by Equ.9 and 8.

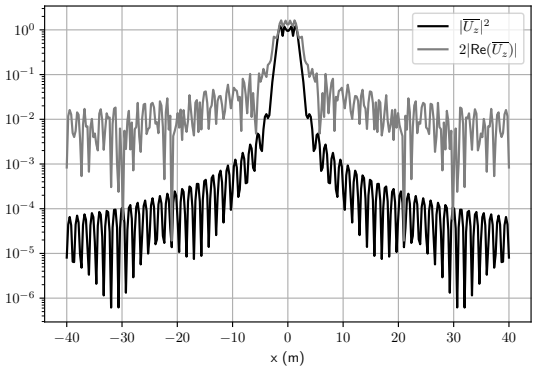

Figure 6: The values of $2\mathrm{Re}\left(\overline{U_z}\right)$ and $|\overline{U_z}|^2$ for a square occulting object.

However, the sensor array does not directly measure the field but rather the intensity I defined as:

$$I(x) = |1 - \overline{U_z}(x)|^2. \tag{23}$$

In conventional imaging, because of the squared modulus, the bandwidth of the intensity is twice as large as the field's bandwidth. The situation is quite different in our case. Indeed, the squared modulus of the field does appear in the intensity expression:

$$I(x) = 1 - 2\mathrm{Re}\left(\overline{U_z}(x)\right) + |\overline{U_z}(x)|^2. \tag{24}$$

In practice, however, the term $|\overline{U_z}|^2$ is quickly negligible compared to $2\mathrm{Re}\left(\overline{U_z}\right)$. To confirm this, we plot in Figure. 6 these two quantities in the simple case of diffraction through a slit, using Fresnel integrals[17] for a Fresnel number of 5, which orresponds to a 10-meter-long satellite observed in the V-band. The ratio also shows that at typically 10 m from the centre, the squared field is 100 times weaker and one really needs excellent SNR conditions to see it. The examples shown in the next section are all with a Fresnel number of about 5, so when $x_{\max}$ will be found higher than 20 m (the distance at which the squared field are well sampled between −10 m and +10 m), we will consider the maximal frequency $f_{\max}$ to be:

$$f_{\max} = \frac{\sqrt{M}}{\pi W_{\mathrm{GEO}}} + \frac{x_{\max}}{R_{\mathrm{GEO}}\lambda_0}. \tag{25}$$

And hence the distance between the measurement points Δx, meeting the Shannon criterion for sampling the chirp function, is:

$$\Delta x = \frac{1}{2f_{\max}}. \tag{26}$$

Otherwise we will have:

$$\Delta x' = \frac{1}{4f_{\max}}. \tag{27}$$

Lastly, if we denote by N_{s} the number of sampling points of the shadow, one has :

$$N_{\mathrm{s}} = \frac{2x_{\max}}{\Delta x}, \tag{28}$$

and we can set the exposure time of the detector as:

$$\Delta t_{\mathrm{s}} = \frac{\Delta x}{v_{\mathrm{o}}}, \tag{29}$$

where v_{o} is the shadow's velocity on the ground.

3.2 Spatial extent

It is easy to see that the diffraction pattern resulting from the diffraction of light by the satellite has an unlimited extent. For example by noticing in Eq. (6) that it is the Fourier transform of a finite support function. But, again, using HG functions automatically limits the diffracted field such as:

$$x_{\max} \approx W_{\mathrm{GEO}}\sqrt{M}. \tag{30}$$

However, there are several parameters that will reduce the extent of the shadow and thereby downgrade the achievable resolution on the object. Among these factors are the spatial and temporal coherence of the light source (the star in our case) and the acceptable noise level. Here we consider that the star is point-like (of infinite spatial coherence) and that the only cause of noise is the photon noise (we neglect the dark current of the photodetector and the stellar background). There is of course a trade-off between the spectral bandwidth and the received flux, and between the sampling and the signal to noise ratio. Yet, our objective here is not to assess the optimal parameters for the best reconstruction but simply to set a realistic framework where the desired resolution ΔX is achieved.

The spatial cut-off due to the spectral extension of the source can be approximated by the following expression, established in reference[31] for a light source at λ_0 and of spectral bandwidth $\Delta\lambda$, written here in normal incidence:

$$x_{\max}^{\Delta_\sigma} = \frac{T}{2} + \frac{1}{\Delta\sigma^2}\sqrt{1 + 2z_{\mathrm{GEO}}\Delta\sigma}, \tag{31}$$

where $\Delta\sigma = \Delta\lambda/\lambda_0^2$.

Then there is the effect of photon noise, it causes that at a certain distance from the centre of the shadow, the diffraction fringes that carry information about the object are drowned in the photon noise.[25] To approximate the distance at which this limitation appears, the level of the fringes must be estimated as a function of the distance to the centre of the shadow. In reference,[31] the author suggests to take as an upper bound its level when the obstacle is an infinite half-plane, in this case we have:

$$\|U_{z_{\mathrm{GEO}}(x)}\|^2 \leq 1 + \frac{\sqrt{\lambda_0 z_{\mathrm{GEO}}}}{\pi(x - T/2)}. \tag{32}$$

The 1 is the normalized intensity without any diffraction while the second part indicates the level of the diffraction fringes. If we denote by N_{ph}^g the number of photons received per measurement without diffraction and N_{ph} the number of photons received per measurement with diffraction, we define the signal to noise ratio as $SNR = \sqrt{N_{\mathrm{ph}}}$. In order to be able to distinguish the fringes without additional noise assumptions, one should at least have:

$$SNR(x) = \sqrt{N_{\mathrm{ph}}(x)} = \sqrt{N_{\mathrm{ph}}^g \frac{\sqrt{\lambda_0 z_{\mathrm{GEO}}}}{\pi(x - T/2)}} \geq 1, \tag{33}$$

that results in:

$$x_{\max}^{\text{shot noise}} \approx \frac{T}{2} + \frac{N_{ph}^g \sqrt{\lambda_0 z_{\mathrm{GEO}}}}{\pi}. \tag{34}$$

Therefore, if we want to achieve the desired resolution on the object, we must at least have:

$$x_{\max} \leq x_{\max}^{\text{shot noise}}, \tag{35}$$

$$x_{\max} \leq x_{\max}^{\Delta\sigma}. \tag{36}$$

If the flux of the starlight is low, the first condition will be limiting; if the flux of the starlight is high, the second condition will be limiting. In order to be able to deduce from these two inequalities the suitable values of $\Delta\sigma$ and m_{v}, we need to detail the expression of $N_{\mathrm{ph}}^{\mathrm{g}}$:

$$N_{\mathrm{ph}}^{\mathrm{g}} = N_0 \Delta\lambda \, \Delta t_{\mathrm{s}} \, \frac{\pi D^2}{4} 10^{-m_{\mathrm{v}}/2.5} \tag{37}$$

where $N_0 \approx 10^5$ photons $\mathrm{m}^{-2}\mathrm{ms}^{-1}\mathrm{nm}^{-1}$ is the photon flux density of Vega (the reference star for apparent magnitudes) and D is the diameter of the telescopes. Moreover, knowing that:

$$\Delta t_s = \left[2v_{\mathrm{o}}\left(\frac{\sqrt{M}}{\pi W_d} + \frac{x_{\max}}{R_d \lambda_0}\right)\right]^{-1}, \tag{38}$$

we find:

$$x_{\max} \leq \frac{T}{2} + N_0 \Delta\lambda \, \Delta t_s \, \frac{D^2}{4} 10^{-m_{\mathrm{v}}/2.5} \sqrt{\lambda_0 z_{\mathrm{GEO}}}, \tag{39}$$

$$x_{\max} \leq \frac{T}{2} + \frac{1}{\Delta\sigma^2}\sqrt{1 + 2z_{\mathrm{GEO}}\Delta\sigma}. \tag{40}$$

Approximating the right-hand side of the second inequality by $T/2 + \sqrt{2z_{\mathrm{GEO}}/\Delta\sigma}$, we get:

$$\Delta\sigma \leq \frac{2z_{\mathrm{GEO}}}{(x_{\max} - T/2)^2}. \tag{41}$$

At this point, we only need to choose D and λ_0 to deduce the values of $\Delta\sigma$ and the maximal magnitude of the star.

4. Reconstruction of the satellite silhouette from simulated data

The field propagation of light is invertible, but the phase information is lost when only its intensity is measured. In order to recover the phase corresponding to the measured amplitude, one must rely on a *Phase Retrieval* numerical algorithm. The oldest such algorithm for Fraunhofer diffraction is a back propagation method proposed by Gerchberg and Saxton.[32] For satellite shadow imaging, Douglas[33] used its version adapted for Fresnel diffraction. Although these projection methods provide rather satisfactory results in many cases, they have several disadvantages. For instance, twin image artefacts may appear, the noise statistics and the quality of the measurement points cannot be taken into account, and only hard constraints on the sought object can be enforced. One way to overcome these limitations is to use modern optimisation methods, by specifying an objective function to be minimised. For instance, the class of gradient descent algorithms has proven to be faster than projection ones,[34] and has been widely adopted in holography.[35] In the following, we present our maximum a posteriori based reconstruction method called NISIM for Non-linear Inversion for Shadow Imaging.

4.1 Maximum a posteriori algorithm

The sought satellite absorption function $(X, Y) \mapsto \overline{U}_0(X, Y)$ is represented as an array of coefficients $\boldsymbol{\alpha} = (\alpha_n)_{0 \leq n \leq M^2}$, which give the projection of a pixel image onto the chosen HG basis such that:

$$\overline{U}_0(\boldsymbol{\alpha}; X, Y) = \sum_{n=0}^{M^2} \alpha_n \phi_n^0(X, Y) \quad \text{for all } X, Y \in [-T/2, T/2], \tag{42}$$

where (ϕ_n^0) are the 2D HG functions at the satellite plane. The diffracted field at the observer plane is hence written:

$$\overline{U}_{z_{\mathrm{GEO}}}(\boldsymbol{\alpha}; x, y) = \sum_{n=0}^{M^2} \alpha_n \phi_n^{z_{\mathrm{GEO}}}(x, y) \quad \text{for all } (x, y) \in \mathbb{R}^2, \tag{43}$$

where $(\phi_n^{z_{\mathrm{GEO}}})$ are the 2D Hermite-Gauss functions at the satellite plane (which are basically just each (ϕ_n^0) propagated analytically over a distance $z = z_{\mathrm{GEO}}$).

The calculated intensity according to the diffraction model is the following:

$$I_{\mathrm{calc}}(\boldsymbol{\alpha}; x, y) = |1 - \overline{U}_{z_{\mathrm{GEO}}}(\boldsymbol{\alpha}; x, y)|^2 \quad \text{for all } (x, y) \in [-x_{\max}, x_{\max}]^2. \tag{44}$$

We denote by I_{mes} the intensity measured by the row of telescopes over time, assuming for convenience that the sampling is the same in the two dimensions x and y.

The objective function to be minimised comprises the measure of the deviation between the model and the measured data $A(\boldsymbol{\alpha})$ defined as:

$$A(\boldsymbol{\alpha}) = \|I_{\mathrm{mes}} - I_{\mathrm{calc}}(\boldsymbol{\alpha})\|_2^2 \tag{45}$$

where $\|\cdot\|_2$ denotes the norm on the measurement array that may include the quality of the measurement points. We append to $A(\boldsymbol{\alpha})$ a regularisation term $R(\boldsymbol{\alpha})$ which provide a prior information on the object sought. The objective function is given by:

$$J(\boldsymbol{\alpha}) = A(\boldsymbol{\alpha}) + \nu R(\boldsymbol{\alpha}). \tag{46}$$

R is chosen in order to be minimal when the coefficients $\boldsymbol{\alpha}$ of the object exactly satisfies the *a priori* assumptions about the object. The minimum of the criterion is therefore a trade-off between concordance with the data and assumptions about the shape of the satellite. The hyperparameter ν allows us to adjust the relative weights between the two terms.

We know *a priori* that the satellite is a completely absorbing opaque object and that it is composed of one single part. A flexible way to add this constraint is the total variation regularization, defined in its modified form as:

$$R(\boldsymbol{\alpha}) = \sum_{k,l} \sqrt{\|\nabla_{X,Y} S(\alpha, X_k, Y_l)\|^2 + \epsilon}, \tag{47}$$

where $\nabla_{X,Y}$ is the spatial gradient in the satellite plane and $\epsilon > 0$ makes the criterion derivable. This regularisation favors smooth solutions while preserving sharp edges, where the norm of the spatial gradient is dominant over ϵ.

In the following, we will apply this reconstruction algorithm in various cases, starting with a narrow-band source.

	$x_{\max}$	$\Delta\lambda$	m_v	Δt_s	N_s	SNR	RMS (noise-free)	RMS_n
$\Delta X_1 = 1\,\text{m}$	22 m	40 nm	8	$1.5e^{-4}$	106	5.24	0.1	0.16
$\Delta X_2 = 0.7\,\text{m}$	31.5 m	15 nm	7	$1.1e^{-4}$	207	4.35	0.06	0.17

Table 1: Parameters of the narrow-band simulations.

4.2 Narrow-band Inverse Crime

All inverse crime simulations are performed for a geostationary satellite of 10 m side length, shown in Fig. 7a. We choose a telescope diameter $D = 0.30\,\text{m}$. We study two different resolutions on the object in the narrow-band: 1 m and 0.7 m, both at $\lambda_0 = 550\,\text{nm}$. We cannot afford to expect a better resolution because of the diameter D, as it restricts the pitch in the shadow plane Δx.

Figure. 7 shows the coefficients of the object in the HG basis corresponding to $\Delta X = 1\,\text{m}$, while Figure. 7c shows the coefficients of the object for $\Delta X = 0.7\,\text{m}$. Figures. 8a and 8b show the discretised and binarized satellite reprojected into the pixel basis. Due to the chosen resolution, the projection is not perfectly smooth and fine details of the object such as the solar panel arms are very blurred. It is the latter objects that we are attempting to retrieve using the reconstruction algorithm.

Given the parameters T and ΔX, the maximum spectral bandwidth $\Delta\lambda$ and the maximum magnitude of the occulted star can be calculated using the inequalities 39 and 40. For $\Delta X_1 = 1\,\text{m}$, we get:

$$m_{\text{v},1}^{\max} \approx 9, \Delta\lambda_1^{\max} \approx 40\,\text{nm}. \tag{48}$$

And for $\Delta X_2 = 0.7\,\text{m}$, we get

$$m_{\text{v},2}^{\max} \approx 7, \Delta\lambda_2^{\max} \approx 15\,\text{nm}. \tag{49}$$

We can hence assume a magnitude 8 and a spectral width of 40 nm for ΔX_1, and a magnitude 7 observed on a spectral channel of 40 nm for ΔX_2. The resulting set of parameters of interest are shown in Table 1.

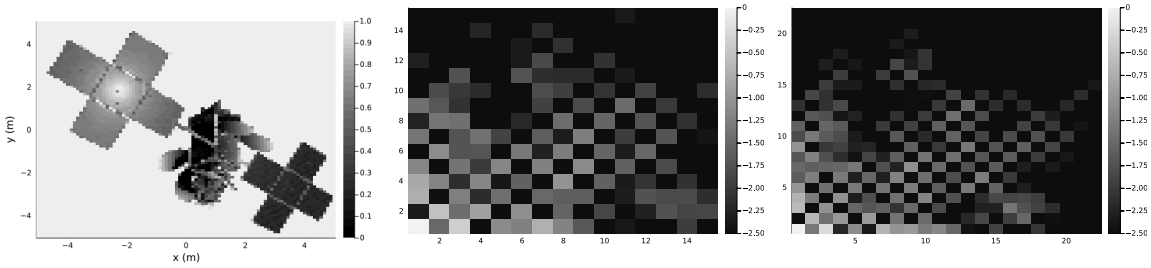

(a) Original discretized satellite.

(b) Satellite's coefficients in the HG basis (logarithmic scale) for ΔX_1.

(c) Satellite's coefficients in the HG basis (logarithmic scale) for ΔX_2.

Figure 7: Discretization of the satellite.

The diffracted intensities and corresponding reconstructions are shown in Table 2. We applied to the intensities a noise corresponding to the PSD of the scintillation calculated in Section. 2.3 (for $V = 30\,\text{m/s}$ and $\text{D} = 30\,\text{cm}$) and a Poisson noise modelling the photon noise. Note that the salt and pepper noise on both intensities is mainly photon noise and not scintillation. For proper comparison, we have also solved both inverse crimes with noiseless intensities but with exactly the same other parameters.

Next, consider the reconstructions using NISIM. The convergence criterion chosen is an absolute deviation of the $\boldsymbol{\alpha}$ vector that is less than 10^{-3}. To evaluate the difference between the various reconstructions, we compute the relative RMS error, shown in Table 1. The two noise-free reconstructions enable to restore well the features of the object, and it results in low RMS errors. As for the noisy inverse crimes (the second and third lines of Table 2), we can visually notice that they replicate well the two references; for both reconstructions with noise, there is no clear decrease in resolution. The first reconstruction at ΔX_1 gives an RMS error of 0.16, while the second at ΔX_2 gives an RMS error of 0.17.

		Measured intensity	Reconstructed object
$\Delta X = 1$ m	Noise-free	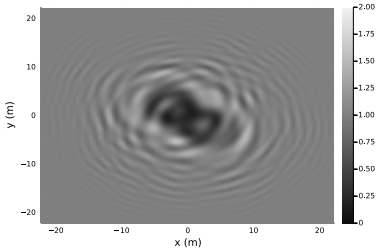	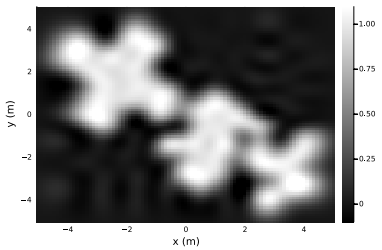
	Noisy	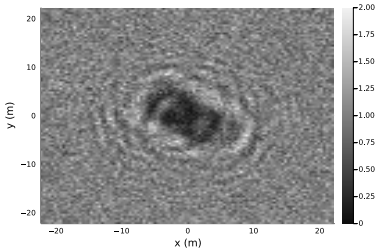	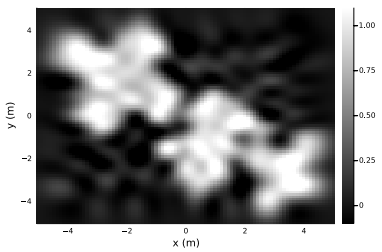
$\Delta X = 0.7$ m	Noise-free	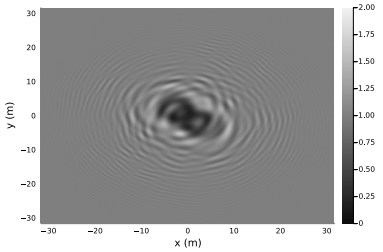	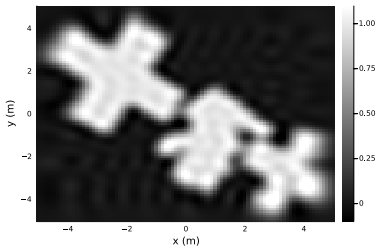
	Noisy	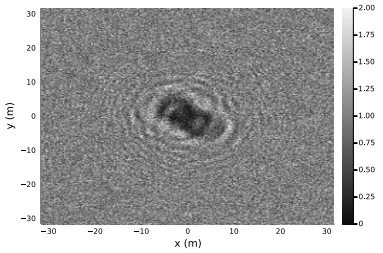	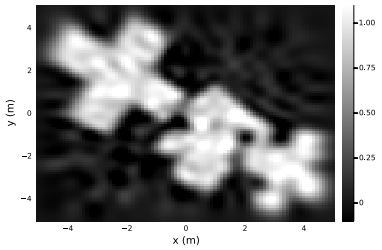

Table 2: Narrow-band reconstructions.

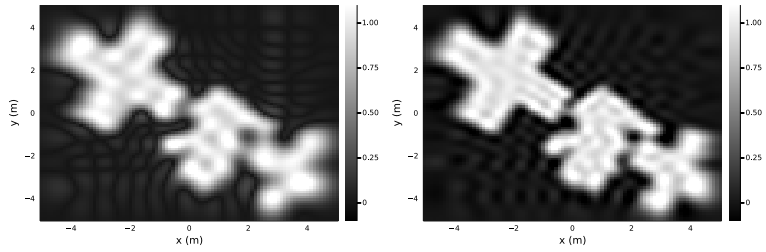

(a) ΔX_1 (b) ΔX_2.

Figure 8: Projection of the object's HG coefficients in the pixel basis.

4.3 Polychromatic Inverse Crime

Even if the reconstructions obtained in the previous paragraph are rather satisfying, one is tempted to measure in parallel on each telescope the intensity diffracted for a different wavelength. This method of spectral diversity is similar in principle to phase-diversity-inspired techniques in holography,[36] where the technical limitations on the size

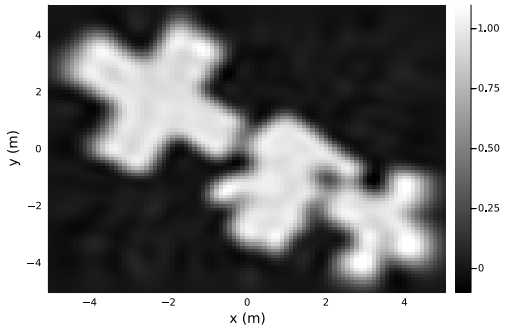

Figure 9: Reconstructed object using polychromatic optimisation.

of the detector pixels can be overcome by varying one of the observation parameters (such as the distance between the object and the detector or the illumination angle). In shadow imaging, one cannot affect the light source nor the object, so the only way is to affect the detector. Increasing the number of spectral channels will allow more of the star's flux to be collected and will increase the SNR, making the inversion more robust to the many sources of noise.

For that purpose, we define a new cost function $J(\boldsymbol{\alpha})$, simply the sum of the criteria for each wavelength:

$$J(\boldsymbol{\alpha}) = \sum_{\lambda_i} \beta_i J_{\lambda_i}(\boldsymbol{\alpha}) \tag{50}$$

where the β_i are real positive coefficients that allow to take into account the discrepancy between the intensities at different wavelengths, due for example to the absorption of the atmosphere or the quantum efficiency of the detector. This straightforward formulation is easily parallelizable, and therefore speeds up the calculations.

To illustrate the gain induced by the use of several spectral channels, we repeat the reconstruction at ΔX_2 but this time on 21 channels of 15 nm between the wavelengths 450 nm and 750 nm. The result using NISIM is shown in Fig. 9. It can be seen that the algorithm has achieved a reconstruction way more sharp and clear than the previous one. The relative RMS error decreased from 0.17 to only 0.11 with multiple wavelengths.

5. Conclusion

In this work about shadow imaging of geostationary satellites, the focus was on the optical propagation of light and the reconstruction algorithm NISIM. The effect of diffraction has been modelled using Hermite-Gauss functions which allow a physical interpretation of the diffraction parameters. Within this framework, a reconstruction algorithm based on a maximum a posteriori was build. The efficiency of the reconstruction has been assessed for two different targeted resolutions on the object. And in both cases, NISIM succeeds in recovering sub-metric details of the object of interest.

The relevance of this work is threefold. First, the analytical study of the two major atmospheric phenomena affecting shadow imaging were investigated. The effect of refraction can be considered negligible when the observation is in a narrow spectral band, and must be compensated between several distant spectral channels. As for scintillation, it causes intensity variations of only a few percent, which can be completely absorbed by the numerical inversion. Second, using the properties of HG functions, the area of interest in the shadow has been determined as a function of the targeted resolution. For this purpose, the losses due to wide spectral bandwidth and the star's magnitude have also been quantified. Along with that, a precise sampling criterion, specific to shadow imaging, has been established. And third, we emphasized in the last subsection the importance of combining several spectral channels in the same measurement points. It allows to increase the effective signal to noise ratio, and has proven to be very effective in decreasing the RMS relative error of the reconstruction.

Our future objectives are to deepen the inversion algorithm, by taking into account for example the variation of the SNR between the center of the shadow and its edges, and by adding a binarity constraint on the object. In parallel to the numerical experiments exposed in this work, we plan to do several laboratory experiments modeling in a small scale the phenomenon.[37]

References

[1] J. Drummond and R. Rast. First Resolved Images of a Spacecraft in Geostationary Orbit with the Keck-II 10 m Telescope. In S. Ryan, editor, *Advanced Maui Optical and Space Surveillance Technologies Conference*, page E21, September 2010.

[2] R. B. Holmes and T. J. Brinkley. Reconstruction of images of deep-space objects using Fourier telescopy. In Timothy J. Schulz and Paul S. Idell, editors, *Digital Image Recovery and Synthesis IV*, volume 3815, pages 11 – 22. International Society for Optics and Photonics, SPIE, 1999.

[3] H. Schmitt, D. Mozurkewich, A. Jorgensen, S. Restaino, J. Armstrong, E. Baines, and R. Hindsley. Simulated Synthesis Imaging of Geostationary Satellites. In *Advanced Maui Optical and Space Surveillance Technologies Conference*, September 2011. Conference Name: Advanced Maui Optical and Space Surveillance Technologies Conference Pages: E76 ADS Bibcode: 2011amos.confE..76S.

[4] D. Mozurkewich, J. Armstrong, R. Hindsley, A. Jorgensen, Sergio Restaino, and Henrique Schmitt. Toward the ground-based imaging of satellites at geosynchronous altitude. In *Advanced Maui Optical and Space Surveillance Technologies Conference*, 09 2011.

[5] H. Schmitt, J. T. Armstrong, E. K. Baines, R. B. Hindsley, A. M. Jorgensen, D. Mozurkewich, S. R. Restaino, G. van Belle, and T. L. Wilson. Analysis of Galileo Style Geostationary Satellite Imaging: Image Reconstruction. In S. Ryan, editor, *Advanced Maui Optical and Space Surveillance Technologies Conference*, page 90, September 2012.

[6] J. T. Armstrong, R. B. Hindsley, H. R. Schmitt, F. J. Vrba, J. A. Benson, D. J. Hutter, and R. T. Zavala. Detection of a geostationary satellite with the Navy Prototype Optical Interferometer. In *Optical and Infrared Interferometry II*, page 77343C, San Diego, California, USA, July 2010.

[7] J. T. Armstrong, E. K. Baines, H. R. Schmitt, S. R. Restaino, J. H. Clark Iii, J. A. Benson, D. J. Hutter, and R. T. Zavala. Multiple-baseline detection of a geostationary satellite with the Navy Precision Optical Interferometer. In *Unconventional Imaging and Wavefront Sensing 2015*, volume 9617, pages 53–60. SPIE, September 2015.

[8] S. R. Restaino, J. T. Armstrong, E. K. Baines, H. R. Schmitt, and James H. C. Iii. Using optical interferometry for GEO satellites imaging: an update. In *Micro- and Nanotechnology Sensors, Systems, and Applications VIII*, volume 9836, pages 14–21. SPIE, May 2016.

[9] J. Young, C. Haniff, D. Buscher, M. Creech-Eakman, and I. Payne. High fidelity imaging of geosynchronous satellites with the MROI. In *Optical and Infrared Interferometry and Imaging V*, volume 9907, pages 836–843. SPIE, August 2016.

[10] R. H. Burns, V. Gamiz, J. J. Dolne, J. Lambert, and S. Long. Shadow imaging of GEO satellites. In *Unconventional Imaging*, volume 5896, page 58960C. International Society for Optics and Photonics, August 2005.

[11] J. L. Elliot. Stellar occultation studies of the solar system. *Annual Review of Astronomy and Astrophysics*, 17(1):445–475, 1979.

[12] P. Tanga and M. Delbo. Asteroid occultations today and tomorrow: toward the GAIA era. *A&A*, 474(3):1015–1022, November 2007. Number: 3 Publisher: EDP Sciences.

[13] D. M. Douglas. *Shadow imaging of geosynchronous satellites*. Thèse de doctorat, Arizona State University, 2014. ISSN: 9781321180817.

[14] D. M. Douglas, B. R. Hunt, and D. G. Sheppard. Shadow imaging of geosynchronous satellites: simulation, image reconstruction, and shadow prediction. In Jean J. Dolne, Thomas J. Karr, and David C. Dayton, editors, *Unconventional Imaging and Wavefront Sensing XII*, volume 9982, pages 93 – 104. International Society for Optics and Photonics, SPIE, 2016.

[15] D. G. Sheppard, D. M. Douglas, B. R. Hunt, and A. Todoki. Recent developments in shadow imaging. In *Advanced Maui Optical and Space Surveillance Technologies Conference*, page 7, 2017.

[16] David G Sheppard, Dennis M Douglas, and Bobby R Hunt. Recent developments in shadow imaging prediction. In *Advanced Maui Optical and Space Surveillance Technologies Conference*, page 7, 2018.

[17] J.W. Goodman. *Introduction to Fourier Optics*. W. H. Freeman, 2017.

[18] C. Aime, É. Aristidi, and Y. Rabbia. The Fresnel Diffraction: A Story of Light and Darkness. *EAS Publications Series*, 59:37–58, 2013.

[19] Kyoji Matsushima and Tomoyoshi Shimobaba. Band-Limited Angular Spectrum Method for Numerical Simulation of Free-Space Propagation in Far and Near Fields. *Opt. Express, OE*, 17(22):19662–19673, October 2009. Publisher: Optica Publishing Group.

[20] Damien P. Kelly. Numerical calculation of the Fresnel transform. *J. Opt. Soc. Am. A, JOSAA*, 31(4):755–764, April 2014. Publisher: Optical Society of America.

[21] Gaurav Dwivedi, Sanjit K. Debnath, Bhargab Das, and Raj Kumar. Revisit to comparison of numerical reconstruction of digital holograms using angular spectrum method and Fresnel diffraction method. *J Opt*, 49(1):118–126, March 2020.

[22] J A Murphy and A Egan. Examples of Fresnel diffraction using Gaussian modes. *Eur. J. Phys.*, 14(3):121–127, May 1993.

[23] H. Kogelnik and T. Li. Laser Beams and Resonators. *Appl. Opt., AO*, 5(10):1550–1567, October 1966. Publisher: Optical Society of America.

[24] R. Borghi, F. Gori, and M. Santarsiero. Optimization of Laguerre-Gauss truncated series. *Optics Communications*, 125(4):197–203, April 1996.

[25] J. Luu, L. Jiang, and B. Willard. Shadow imaging efforts at MIT Lincoln Laboratory. In C. Paxson, H. Snell, J. Griffin, K. Kraemer, S. Price, M. Kendra, and D. %P. E37 Mizuno, editors, *Advanced Maui Optical and Space Surveillance Technologies Conference*, page E34, January 2008.

[26] H. Labriji, O. Herscovici-Schiller, and F. Cassaing. Computation of the lateral shift due to atmospheric refraction *(Forthcoming). Astron. Astrophys.*, 2022.

[27] F. Roddier. V The Effects of Atmospheric Turbulence in Optical Astronomy. In *Progress in Optics*, volume 19, pages 281–376. Elsevier, 1981.

[28] A. N. Kolmogorov. The Local Structure of Turbulence in Incompressible Viscous Fluid for Very Large Reynolds Numbers. *Proceedings: Mathematical and Physical Sciences*, 434(1890,):9–13, 1991.

[29] J-M. Conan, G. Rousset, and P-Y. Madec. Wave-front temporal spectra in high-resolution imaging through turbulence. *JOSA A*, 12(7):1559–1570, July 1995. Publisher: Optical Society of America.

[30] D. Dravins, L. Lindegren, E. Mezey, and A. T. Young. Atmospheric Intensity Scintillation of Stars. III. Effects for Different Telescope Apertures. *Publications of the Astronomical Society of the Pacific*, 110(747):610–633, May 1998.

[31] F. Soulez. Gauging diffraction patterns: field of view and bandwidth estimation in lensless holography. *Appl. Opt.*, 60(10):B38, April 2021.

[32] R. Gerchberg. A practical algorithm for the determination of phase from image and diffraction plane pictures. *undefined*, 1972.

[33] D. M. Douglas, B. R. Hunt, and D. Sheppard. Resolution limits for shadow imaging of geosynchronous satellites: analytic and simulated approaches. In Jean J. Dolne and Rick P. Millane, editors, *Unconventional and Indirect Imaging, Image Reconstruction, and Wavefront Sensing 2017*, page 24, San Diego, United States, September 2017. SPIE.

[34] J. R. Fienup. Phase retrieval algorithms: a comparison. *Appl. Opt., AO*, 21(15):2758–2769, August 1982. Publisher: Optica Publishing Group.

[35] C. Fournier, L. Denis, E. Thiebaut, T. Fournel, and M. Seifi. Inverse problem approaches for digital hologram reconstruction. In *Three-Dimensional Imaging, Visualization, and Display 2011*, volume 8043, pages 234–247. SPIE, May 2011.

[36] P. Bao, F. Zhang, G. Pedrini, and W. Osten. Phase retrieval using multiple illumination wavelengths. *Opt. Lett., OL*, 33(4):309–311, February 2008. Publisher: Optica Publishing Group.

[37] H. Labriji, O. Herscovici-Schiller, and F. Cassaing. Shadow Imaging of Geostationary Satellites: experimental demonstration with accurate polychromatic modelling of diffraction and atmospheric disturbancesn. In *Advanced Maui Optical and Space Surveillance Technologies Conference*, 2022.